THE NATURE OF DIFFUSE IONISED GAS IN STAR-FORMING GALAXIES

Постникова Вера Константиновна (ФФ МГУ, ГАИШ МГУ)

VoLGa, 02 мая 2024 г.

The nature of diffuse ionised gas in star-forming galaxies

William McClymont,[1,2]★ Sandro Tacchella,[1,2] Aaron Smith,[3] Rahul Kannan,[4] Roberto Maiolino,[1,2] Francesco Belfiore,[5] Lars Hernquist,[6] Hui Li[7] and Mark Vogelsberger[8]

[1]Kavli Institute for Cosmology, University of Cambridge, Madingley Road, Cambridge CB3 0HA, UK
[2]Cavendish Laboratory, University of Cambridge, 19 JJ Thomson Avenue, Cambridge CB3 0HE, UK
[3]Department of Physics, The University of Texas at Dallas, Richardson, Texas 75080, USA
[4]Department of Physics and Astronomy, York University, 4700 Keele Street, Toronto, ON M3J 1P3, Canada
[5]INAF — Arcetri Astrophysical Observatory, Largo E. Fermi 5, I-50125, Florence, Italy
[6]Center for Astrophysics | Harvard & Smithsonian, 60 Garden Street, Cambridge, MA 02138, USA
[7]Department of Astronomy, Tsinghua University, Beijing 100084, People's Republic of China
[8]Department of Physics and MIT Kavli Institute for Astrophysics and Space Research, 77 Massachusetts Avenue, Cambridge, MA 02139, USA

ABSTRACT
We present an analysis of the diffuse ionised gas (DIG) in a high-resolution simulation of an isolated Milky Way-like galaxy, incorporating on-the-fly radiative transfer and non-equilibrium thermochemistry. We utilise the Monte-Carlo radiative transfer code COLT to self-consistently obtain ionisation states and line emission in post-processing. We find a clear bimodal distribution in the electron densities of ionised gas (n_e), allowing us to define a threshold of $n_e = 10\,\mathrm{cm}^{-3}$ to differentiate DIG from H II regions. The DIG is primarily ionised by stars aged $5-25\,\mathrm{Myr}$, which become exposed directly to low-density gas after H II regions have been cleared. Leakage from recently formed stars ($< 5\,\mathrm{Myr}$) is only moderately important for DIG ionisation. We forward model local observations and validate our simulated DIG against observed line ratios in [S II]/Hα, [N II]/Hα, [O I]/Hα, and [O III]/Hβ against $\Sigma_{H\alpha}$. The mock observations not only reproduce observed correlations, but also demonstrate that such trends are related to an increasing temperature and hardening ionising radiation field with decreasing n_e. The hardening of radiation within the DIG is caused by the gradual transition of the dominant ionising source with decreasing n_e from 0 Myr to 25 Myr stars, which have progressively harder intrinsic ionising spectra primarily due to the extended Wolf-Rayet phase caused by binary interactions. Consequently, the DIG line ratio trends can be attributed to ongoing star formation, rather than secondary ionisation sources, and therefore present a potent test for stellar feedback and stellar population models.

Key words: radiative transfer – galaxies: ISM – ISM: structure – ISM: lines and bands – HII regions – galaxies: stellar content

However, a significant fraction of the ionised gas within the ISM of star forming galaxies is in the form of diffuse ionised gas (DIG), which is lower density than a typical H II region and ~ 2000 K hotter (Madsen et al. 2006). It is observed in edge-on galaxies as extraplanar gas extending on kpc scales above the thin disk and in face-on galaxies as lower surface brightness regions (Levy et al. 2019). The DIG contributes around half of the Hα emission in star-forming galaxies, which implies that the DIG contributes substantially to the overall energy budget of the ionised phase of the ISM (Oey et al. 2007; Tacchella et al. 2022). The most obvious candidate for the source of DIG ionisation is leaking radiation from H II regions, as the DIG is often observed to be spatially associated with H II regions (Levy et al. 2019; Belfiore et al. 2022), however this has not been a universally accepted conclusion (Seon 2009).

To further complicate the picture, observations of metal line emission in the DIG have found that the line ratios [N II]$\lambda6585$ Å/Hα, [S II]$\lambda6718,33$ Å / Hα, [O I]$\lambda6302$ Å / Hα, and [O III]$\lambda5008$ Å / Hβ increase with decreasing surface brightness, implying that they increase as ionised gas becomes more diffuse (Hill et al. 2014). Photoionisation modelling can explain the [N II]/Hα, [S II]/Hα, and [O I]/Hα trends as a result of radiation leaking from an H II region into and ionising low-density gas (Belfiore et al. 2022).

However, the [O III]/Hβ trend is more difficult to explain. The ionisation energy of O II is 35.1 eV, which would imply that the radiation field becomes significantly harder as gas becomes more diffuse. While radiation from H II regions hardens as it leaks due to the photoionisation cross section of H I decreasing with energy, this effect has so far not been sufficient to reproduce the observed line ratios in photoionisation models (Wood & Mathis 2004; Barnes et al. 2015). Alternatively, additional sources of heating in the DIG may be sufficient to shift the emissivity ratio of [O III]/Hβ enough to reproduce the observed line ratios (Rand 1998). Potential mechanisms for this heating include cosmic rays (Vandenbroucke et al. 2018), photoelectric heating of dust grains (Reynolds & Cox 1992), or turbulence (Binette et al. 2009).

A secondary hard ionisation source in the DIG could cause an increased abundance of O III and therefore explain the observed line ratios. The most promising secondary ionisation source is the contribution of stars with masses $0.8 - 8$ M$_\odot$ in evolutionary phases after the asymptotic giant branch stage (post-AGB), also called hot low-mass evolved stars (HOLMES). These stars have a hard ionising spectrum, and could provide a significant contribution to the budget of high-energy photons while still maintaining a low overall contribution to the total emission of ionising photons (Flores-Fajardo et al. 2011). The importance of old stars in ionising the ISM of elliptical and lenticular galaxies has been well studied (Sarzi et al. 2010; Singh et al. 2013), but their contribution has also been invoked by Zhang et al. (2017) to explain the line ratio trends in star-forming galaxies observed in the MaNGA survey (Bundy et al. 2015).

The recent study by Belfiore et al. (2022) examines ionisation sources within the DIG by utilising emission line maps from face-on, star-forming galaxies in the PHANGS-MUSE survey (Emsellem et al. 2022). This work offers the most detailed perspective of the DIG to date, enabling us to resolve the ISM in emission at scales of tens of parsecs. Furthermore, this work also supports the idea that the observed line ratios are significantly influenced by HOLMES.

These conclusions regarding the DIG conditions are based on relatively simple photoionisation models. While such models are

In this work, we aim to address the theoretical shortcomings by employing the recently developed capability for metal ionisation and line emission in the Monte Carlo radiative transfer (MCRT) Cosmic Lyα Transfer code (COLT; Smith et al. 2015, 2019, 2022) to self-consistently model the resolved optical metal line emission from a simulated Milky Way-like (MW-like) galaxy. Our approach builds upon the work of Tacchella et al. (2022), wherein this model was demonstrated to effectively reproduce realistic Balmer line emission from the DIG.

Utilizing this methodology, our study is focused on addressing the following questions:

(i) Do the observed trends in the DIG align with those predicted by a purely theoretical definition of the DIG?

(ii) Are the variations in line ratios within the DIG primarily influenced by changes in ionic abundances, or by line emissivity due to temperature variations?

(iii) What are the respective contributions of H II region leakage, old stars, and shocks in generating these line ratios?

2.1 Isolated MW simulation

In this study, we utilize a high-resolution simulation of a galaxy designed to resemble the Milky Way, characterized by a halo mass of $M_{\rm halo} = 1.5 \times 10^{12}\,{\rm M_\odot}$, stellar bulge and disk mass of $M_{\rm stars} = 6.2 \times 10^{10}\,{\rm M_\odot}$, and gas mass of $M_{\rm gas} = 9 \times 10^9\,{\rm M_\odot}$. This simulation was previously presented by Kannan et al. (2020) and Kannan et al. (2021), but we summarise the most relevant details below. The simulation employs AREPO-RT (Kannan et al. 2019), which is an extension of the moving mesh hydrodynamic code AREPO (Springel 2010; Weinberger et al. 2020)[1]. The sub-grid models, which are crucial for capturing star formation and feedback processes, are described in Marinacci et al. (2019) and Kannan et al. (2020). Important projected quantities derived from the simulation are illustrated in Fig. 1.

scale length (Hernquist 1990). The stellar disk follows a radial exponential profile with an effective radius $R_{\rm eff} = 2\,{\rm kpc}$ and a vertical sech^2 profile with a 300 pc scale height, and the initial stars are assigned an age of 5 Gyr. The gas disk also follows a radial exponential profile with the same effective radius as the stellar disk. It is vertically distributed in hydrostatic equilibrium, starting with an initial temperature of 10^4 K and a metallicity of $1\,{\rm Z_\odot}$. The idealised nature of the simulation and lack of cosmological environment could lead to unrealistic gas metallicities, so the creation of new metals is turned off. This has the benefit of isolating our investigation of the ionisation and distribution of the DIG from the effects of metallicity gradients and metallicity evolution between snapshots. The simulation runs for 1 Gyr and, following an initial starburst, reaches a quasi-equilibrium state around ~ 200 Myr.
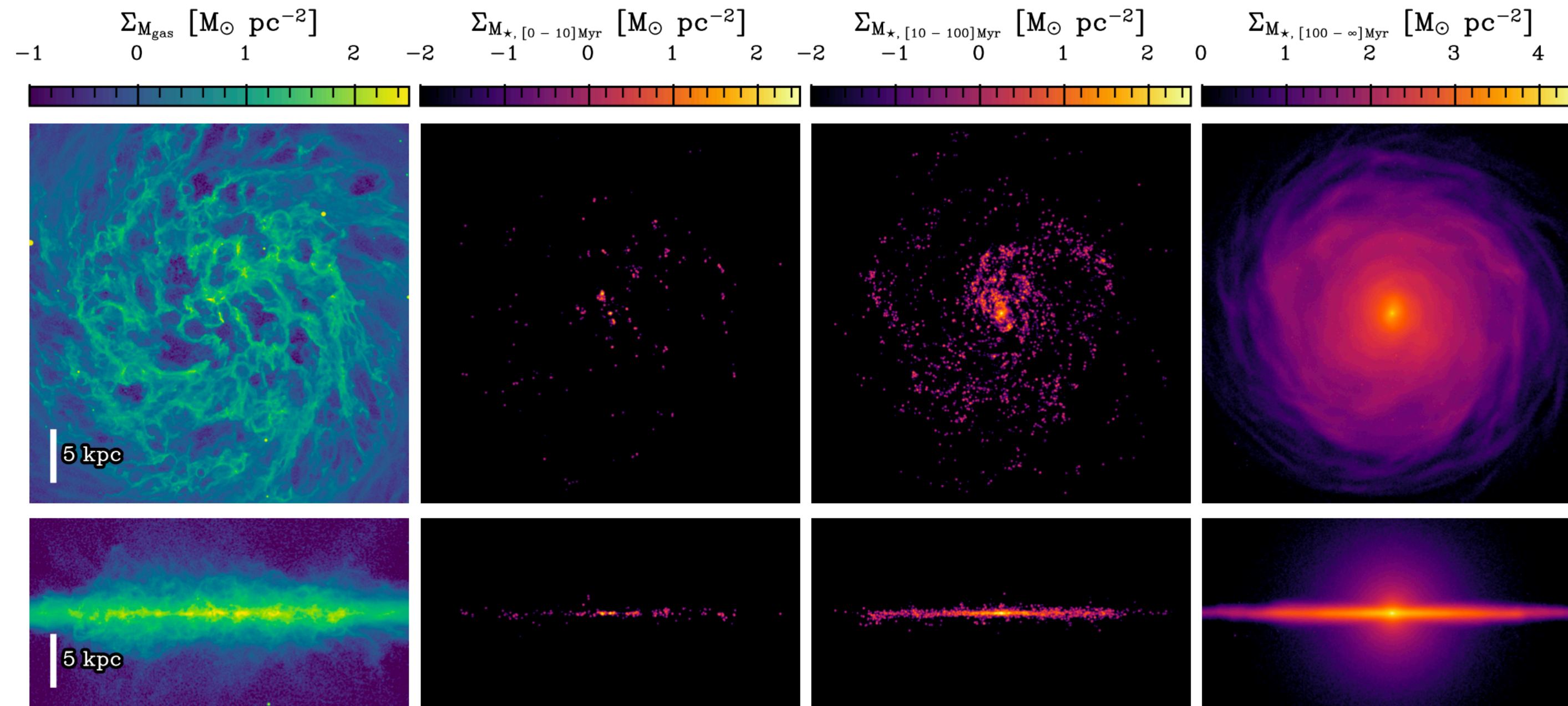

Figure 1. Projected properties of the MW-like simulation at 713 Myr, including 50 pc smoothed surface density maps displayed from left to right of gas mass, stellar mass in young stars ([0 − 10] Myr), stellar mass in intermediate-aged stars ([10 − 100] Myr), and stellar mass in older stars ([100 − ∞] Myr). The maps highlight the stochastic nature of star formation, which is especially evident in the strongly non-uniform distribution of recent star formation observed over 10 Myr timescales.

2.2 Radiative transfer of ionising photons

To accurately predict line emission from the simulation, we must know the relative ionic abundances in each gas cell. The isolated MW-like simulation tracks the relative abundances of H_2, $H\,\textsc{i}$, $H\,\textsc{ii}$, $He\,\textsc{i}$, $He\,\textsc{ii}$, $He\,\textsc{iii}$, which in theory makes it possible for us to directly calculate the Balmer line emission. However, using the on-the-fly ionisation state abundances for Balmer line emission estimation can result in observed luminosities that are an order of magnitude too high. This discrepancy is primarily due to very young $H\,\textsc{ii}$ regions within the simulation lacking a fully resolved substructure in terms of density and temperature, as discussed in Smith et al. (2022).

Consequently, it is necessary to recompute the ionisation states of H and He using a post-processing approach. Moreover, considering our interest in spatially- and spectrally-resolved line emission from metals, a post-processing approach is also essential because the relative abundances of metal ions are not tracked on-the-fly. We employ COLT to perform MCRT of ionising radiation and thereby obtain ionisation states for each simulated gas cell. The pri-

We now briefly describe the ionisation equilibrium calculations. Ionising photons are primarily emitted by young, massive stars, while the star particles in the simulation represent initial mass function (IMF) averaged stellar populations. These sources are characterized by SEDs derived from the Binary Population and Spectral Synthesis (BPASS) model (v2.2.1; Eldridge & Stanway 2009; Eldridge et al.
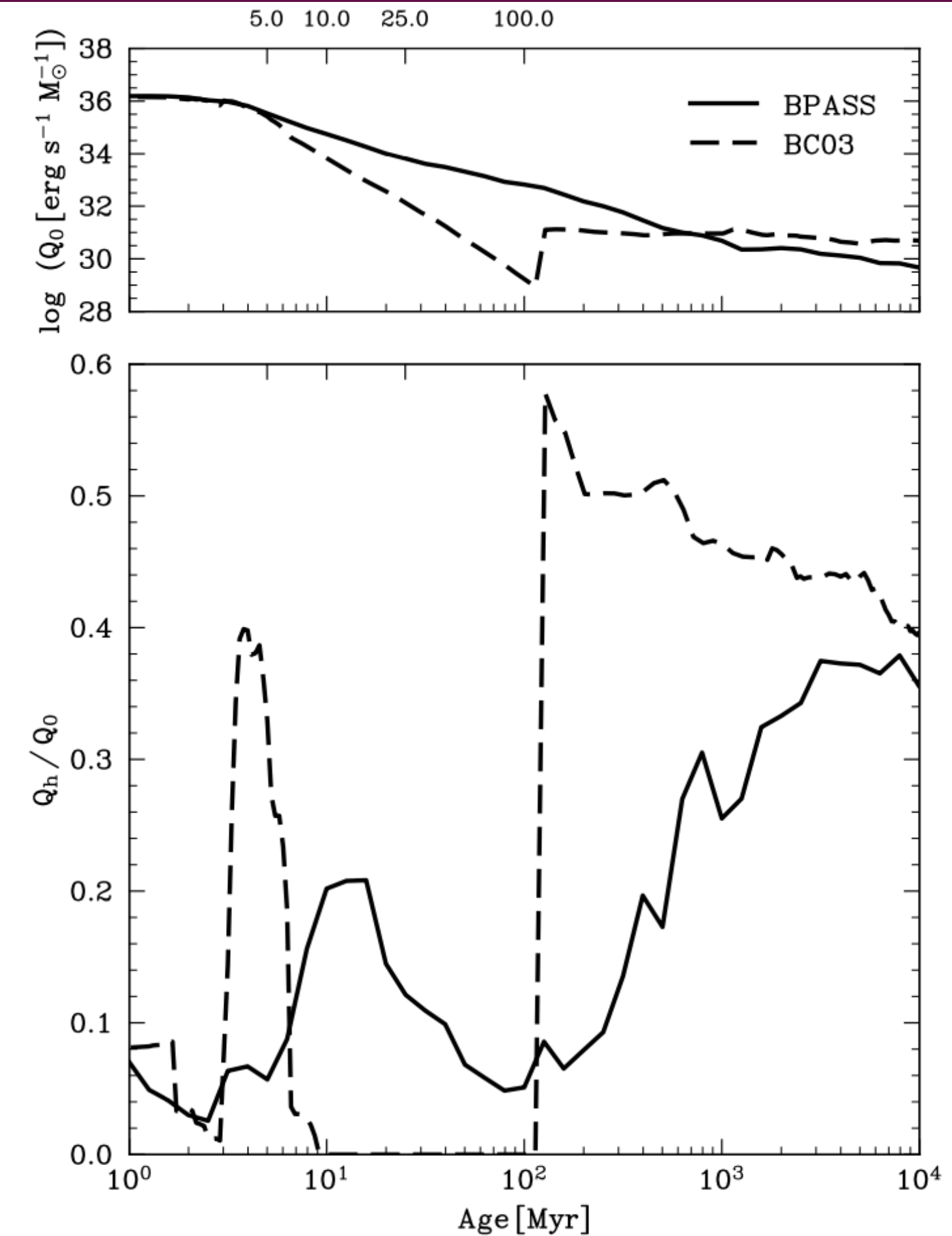

Figure 12. The intrinsic properties of stars in the simulation. We use the BPASS library (solid lines), however we plot the BC03 properties (dashed lines) as a comparison. *Top:* The ionising emissivity of stars as a function of age. The youngest stars dominate the production of ionising photons. *Bottom:* The rate of O^{++} ionising photons (>35.12 eV) from stars, Q_h, divided by the rate of $H\,\textsc{i}$ ionising photons (>13.6 eV) from stars, Q_0. The hardness of the ionising radiation from stars in the BPASS library peaks from 5 to 25 Myr (a shorter and earlier hardness peak is also seen in BC03). This peak explains importance of these stars in driving a hard radiation field in the DIG, when considered alongside the low-density environments in which these stars reside (Fig. 11).

2.3 Radiative transfer of emission line photons

After establishing the ionic abundances for each cell in the simulation, our next step is to calculate the line emission that arises from this ionisation state distribution. Fundamentally, this process still involves solving for the radiative transfer of photons through the ISM. However, a crucial distinction here is that the source of these photons is diffuse in nature; i.e. we are now sampling emission-line photons from gas cells rather than ionising photons originating from stars. This shift to line radiative transfer means that the included physics is more focused; e.g. we employ continuous frequency tracking with Doppler-shifting between comoving gas frames for accurate spatially- and spectrally-resolved synthetic observations.

In the process of performing MCRT for emission lines and generating emission-line maps, we again utilise the COLT code. Examples of the resulting surface brightness images for the Hα, [N II], and [O III] lines are illustrated in Fig. 2.

To accurately determine the luminosity of the gas cells for a given emission line, it is essential to account for the two primary mechanisms through which emission-line photons are emitted: collisional excitation and recombination. Collisional excitation occurs when an electron collides with an atom, transferring energy that excites another bound electron to a higher energy state. The subsequent radiative deexcitation emits a line photon. Recombination, on the other hand, involves the capture of a free electron by an ionised atom, resulting in the release of line photons as the system cascades to lower energy states. For most emission lines, one of these channels dominates the other to such an extent that lines are often referred to as collisionally excited lines (CELs) or recombination lines (RLs). This is certainly the case for the emission lines we examine in this work: Hα, Hβ, [N II], [S II], [O I], and [O III]. For the RLs Hα and Hβ, we consider the dominant recombination channel and the minor collisional excitation channel. The metal lines in this work are all CELs and we only consider the dominant collisional channel for them. Still, information from multiple emission lines is highly complementary for understanding the conditions within the ISM and DIG of galaxies, owing to the specific density, temperature, and metallicity environmental dependencies.

The RL and CEL channels pose distinct challenges in our modelling approach. Let us first consider a recombination line, which has
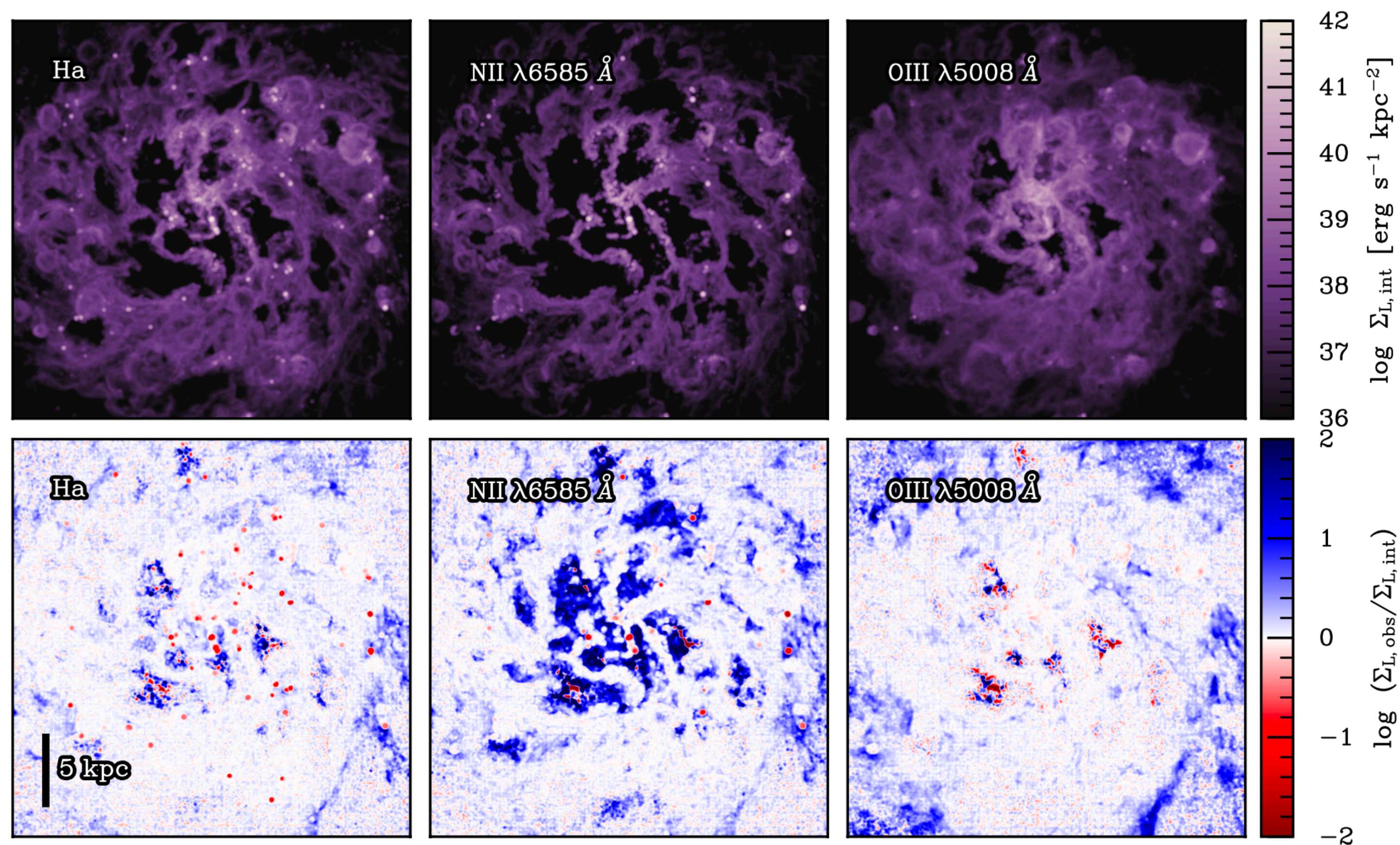

Figure 2. Hα, [N II], and [O III] maps for our MW-like simulation at 713 Myr. Maps have been smoothed by 100 pc to improve visibility. *Top:* The intrinsic surface brightness of each emission line, $\Sigma_{L,int}$. *Bottom:* The ratio of observed-to-intrinsic surface brightness in each pixel. The compact, bright regions around recent star formation are heavily attenuated due to the high concentration of dust. On the other hand, low surface brightness regions are boosted due to dust scattering photons into the line of sight.

3 COMPARISON TO OBSERVATIONS

In this section, we show that our mock observed line ratios match observations of local star-forming galaxies. In Section 3.1, we show that the surface brightness profiles of our simulated emission lines match those in the SDSS/MaNGA survey (Bundy et al. 2015). In Section 3.2, we show that when treating our mock observations as an observer would when analysing the DIG, we recover the the observed line ratio trends of galaxies in the PHANGS-MUSE survey (Emsellem et al. 2022).

3.1 Radial profiles from SDSS/MaNGA

The SDSS/MaNGA survey (Bundy et al. 2015) provides spatially-resolved emission line maps for a large sample of galaxies. By comparing the surface brightness profiles of MaNGA galaxies to those generated from our simulation with COLT, we can confirm that we are producing realistic mock observations.

Previous comparisons between the Hα and Hβ surface brightness profiles from our MW-like simulation and the MaNGA observations have shown good agreement (Tacchella et al. 2022). In this study, we extend this comparison to include metal emission lines, using the same subset of 52 MaNGA-observed galaxies that resemble the MW. Galaxies in the sample were selected based on specific criteria: elliptical Petrosian photometry stellar masses from the NASA-Sloan Atlas (Blanton et al. 2005, 2011) in the range $\log(M_\star/M_\odot) = 10.6$–10.9 and SFRs calculated with Hα to be between SFR/($M_\odot$ yr^{-1}) = 0.5–5.0. Galaxies were rejected from the sample if labelled with DAP

Fig. 3 shows a comparison of the Hα, Hβ, and [O III] surface brightness profiles between the MW-like selected MaNGA galaxies and our simulations (based on four snapshots). The surface brightness profiles from our simulation closely match MaNGA, which strengthens our confidence in the simulation's ability to accurately replicate line emission from a MW-like galaxy.
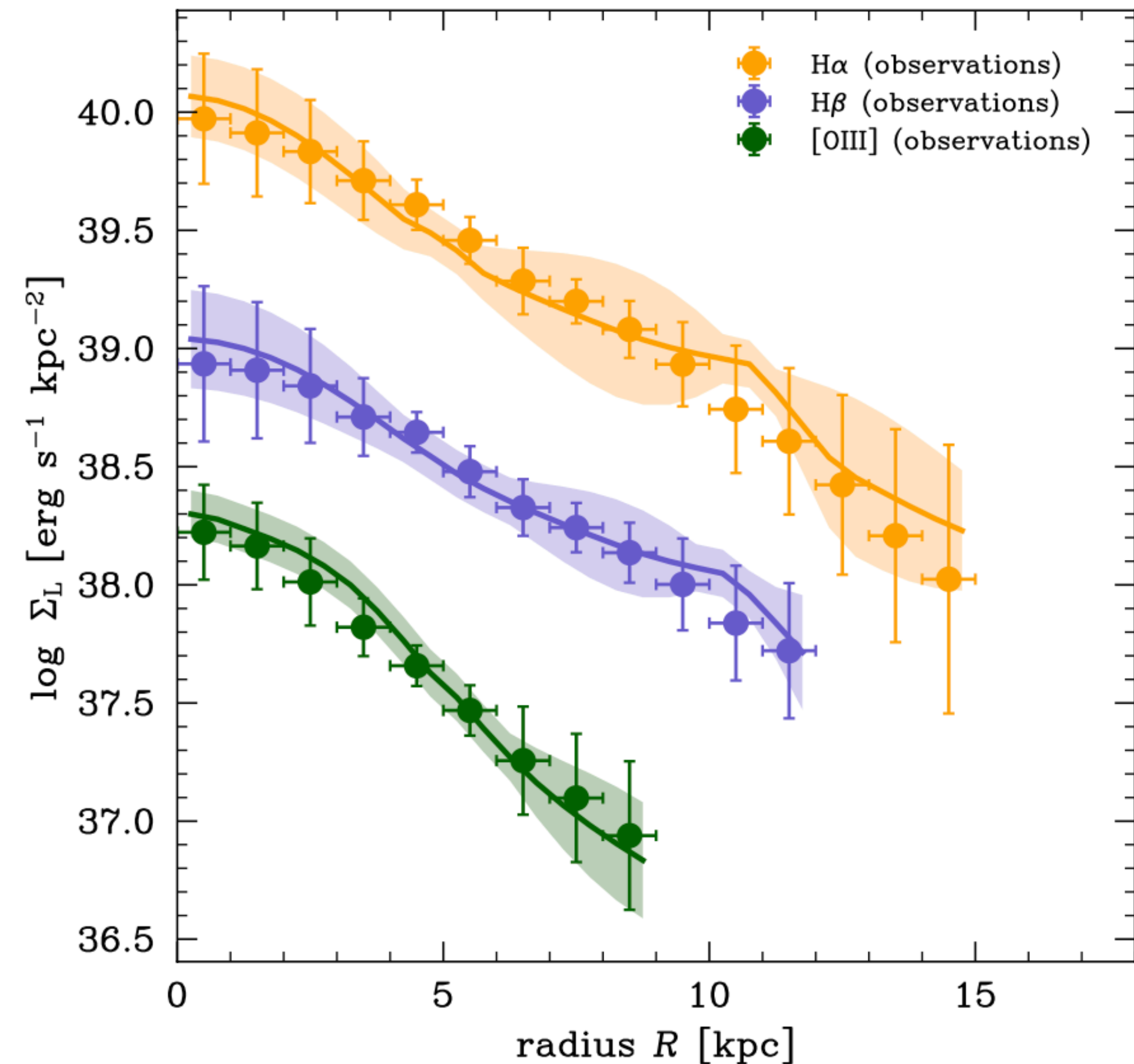

Figure 3. Comparison of median radial surface brightness profiles of Hα, Hβ, and [O III] between the sample of MW-like galaxies from MaNGA and four snapshots of our simulated MW galaxy. The errorbars and shaded regions represent the 16–84$^{\text{th}}$ percentile scatter for the MaNGA sample and sampled simulation snapshots respectively. The Hα, Hβ, and [O III] profiles are normalised to a total luminosity of 10^{42} erg s^{-1}, 10^{41} erg s^{-1}, and 10^{40} erg s^{-1}, respectively. Our MW simulation modelling successfully produces realistic surface brightness profiles.

3.2 Line ratios from MUSE

While the agreement of radial surface brightness profiles with MaNGA data helps give us confidence that our post-processing approach has produced physically reasonable emission line maps, the definitive test is to recreate the specific observational phenomena we are seeking to explain. In particular, we want to reproduce the trends observed between line ratios and Hα surface brightness ($\Sigma_{H\alpha}$) in the DIG as reported in Belfiore et al. (2022).

To achieve this, we must carefully account for observational effects to generate mock MUSE emission line maps and then analyse them as an observer. In general we follow the methods from Belfiore et al. (2022).

We now outline the procedure. First, we employ COLT to model observed Hα emission line maps at 10 pc resolution. We then apply a Gaussian PSF with a FWHM of 60 pc, comparable to the PHANGS-MUSE sample of galaxies, and rebin to a resolution of 20 pc, equivalent to the 0.2″ pixels for the PHANGS-MUSE sample. Finally, we introduce realistic noise levels by adding random Gaussian fluctuations to each spaxel with a mean of 2×10^{37} erg s^{-1} kpc^{-2}. This gives an average SNR of ~ 3 in spaxels with $\Sigma_{H\alpha} = 6 \times 10^{37}$ erg s^{-1} kpc^{-2}, which again matches the PHANGS-MUSE data (Emsellem et al. 2022).

Fig. 4 shows the selected H II regions overlaid on the mock MUSE Hα emission line map. With our H II regions selected, we can mask them out and identify the remaining spaxels as part of the DIG. To further increase the SNR, particularly for the fainter metal lines, we again rebin the DIG spaxels to 140 pc resolution, equivalent to 1.4″ spaxels in the PHANGS-MUSE sample (Belfiore et al. 2022). Finally, we utilised the VORBIN package on the diffuse pixels to achieve a minimum Hα SNR of 60. VORBIN uses a Voronoi binning technique to combine lower S/N spaxels together to increase the SNR at the expense of spatial resolution.
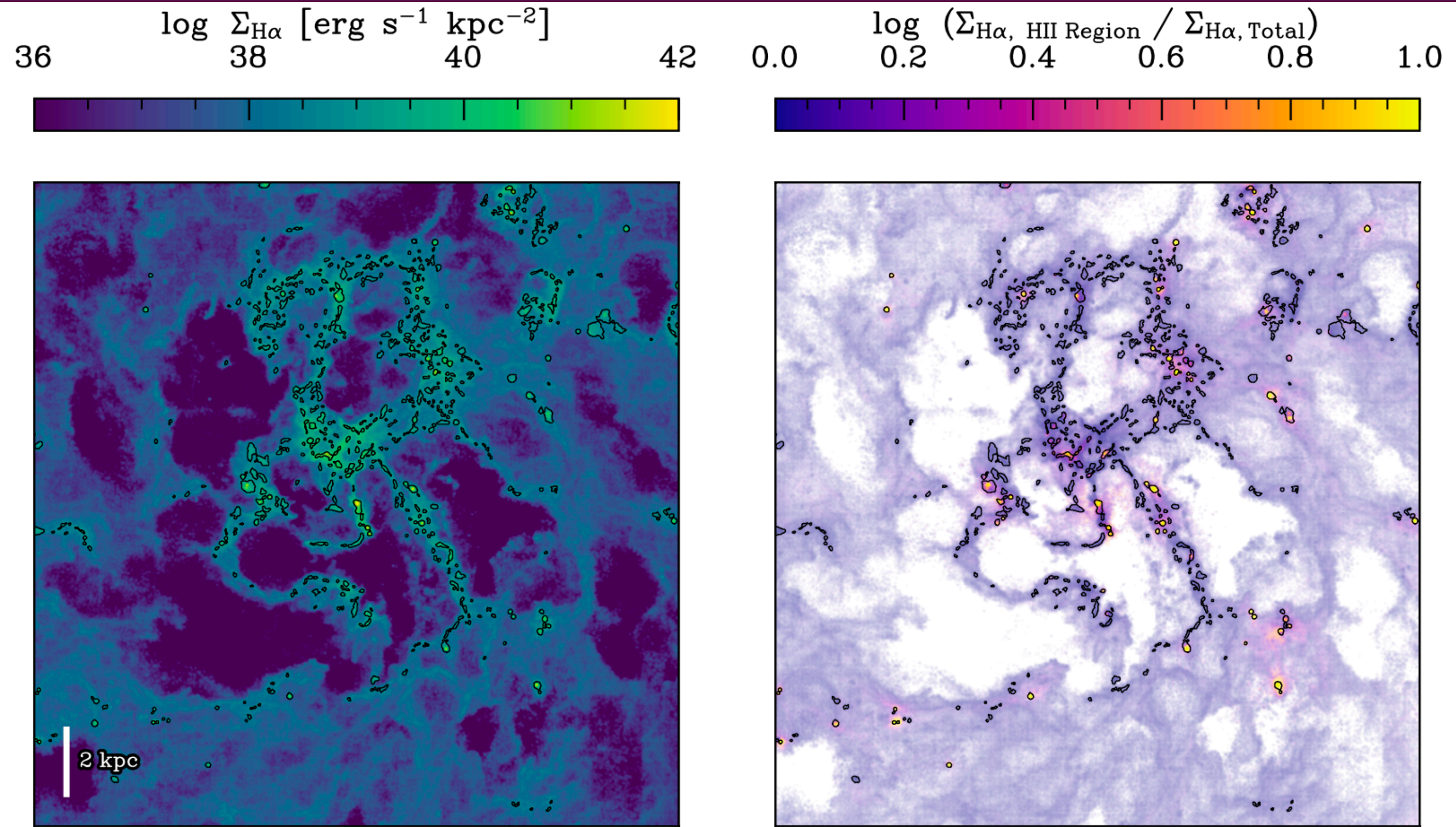

Figure 4. Observational selection of the DIG. *Left:* A mock MUSE Hα emission line map with black contours illustrating the H II regions selected using the dendrogram method. *Right:* The fraction of Hα emission in a spaxel from gas with a density larger than $n_e = 10$ cm^{-3}, our theoretical demarcation between H II regions and the DIG. The image transparency is based on the Hα surface brightness. The dendrogram selection includes most spaxels which are dominated by the theoretically defined H II regions, however it also selects a significant number of DIG dominated spaxels.

Using these binned spaxels, we plot [S II]/Hα, [N II]/Hα, [O I]/Hα, and [O III]/Hβ line ratios as a function of $\Sigma_{H\alpha}$ in the DIG for our MW-like simulation in Fig. 5. The mock observations were split into five radial bins from from [0−16] kpc and the line ratio profile was calculated for each. In order to compare the line ratio trends between the radial bins and across snapshots, which have different average line ratios, each of the profiles is normalised such that the average line ratio in each radial bin is unity. The trendline represents the median values from four snapshots with five radial bins each.

We decided to show the trends in this way to facilitate a direct comparison with the PHANGS-MUSE observations, which are already split into five radial bins to isolate the effects of a metallicty gradient (Belfiore et al. 2022). We compare our results to the PHANGS-MUSE galaxies which meet our MW-like criteria, which is as above; stellar masses of $\log(M_\star/M_\odot) = 10.6–10.9$ and SFR/$(M_\odot \, yr^{-1}) = 0.5–5.0$. This leaves us with a sample of six galaxies.

Our analysis reveals that the [S II]/Hα, [O I]/Hα, and [O III]/Hβ line ratio trends in our simulation agree well with those observed in the MW-like PHANGS-MUSE galaxies. Specifically, we capture the increase in these line ratios with decreasing surface brightness.
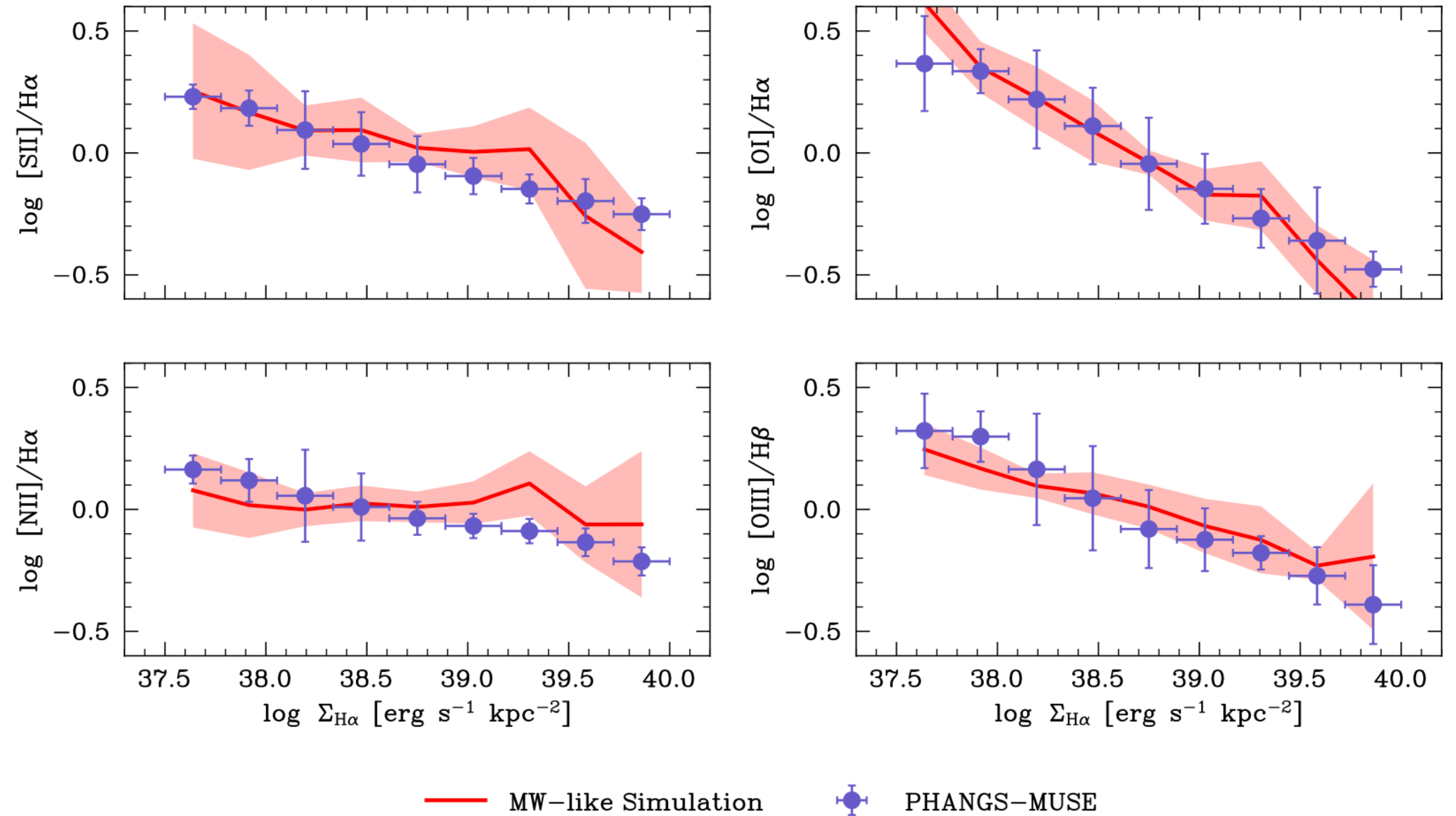

Figure 5. An observers view of the [S II]/Hα, [N II]/Hα, [O I]/Hα, and [O III]/Hβ line ratios as functions of $\Sigma_{H\alpha}$ in the DIG for MW-like PHANGS-MUSE observed galaxies (Belfiore et al. 2022) and our simulation. For both, each galaxy was divided into five radial bins and the DIG-dominated spaxels were selected using morphological methods. The line ratio profiles were calculated from these spaxels and normalised such that the average line ratio in each radial bin is unity, to facilitate direct comparison of line ratio trends across galaxies. The data points and trendline represent the median profiles (errorbars and shaded regions represent the 16–84th percentile scatter)for the PHANGS-MUSE galaxies and four simulation snapshots with five radial bins each. The trends of our simulation generally agree with those in observed MW-like galaxies, giving us confidence that our simulated DIG mirrors the physical conditions of the DIG in reality. While the [N II]/Hα ratio is consistent within the scatter, it appears flatter than observations, possibly because we do not capture the full variety of MW-like galaxies (see Section 3.2).

4 PHYSICS OF THE DIG

Having shown that we are able to reproduce key observational features of the DIG, we now seek to understand the physical properties of the ISM and radiative transfer effects that drive the observed line ratio trends. We begin in Section 4.1 by discussing our approach to

4.1 Physical properties

As we have seen, the DIG is usually defined in high-resolution emission-line maps using morphological analysis. Other definitions have been used, particularly for lower resolution data, such as selecting spaxels based on the equivalent width of $H\alpha$. These definitions lack a robust theoretical foundation as the methods are rooted in phenomenology rather than the intrinsic properties/characteristics of the gas.

In Fig. 6, we plot the intrinsic and observed $H\alpha$ luminosity as a function of n_e. There is a striking bimodality, with two peaks at $0.1 - 1\,\mathrm{cm^{-3}}$ and $10^2 - 10^3\,\mathrm{cm^{-3}}$ contributing the bulk of the observed $H\alpha$ emission. This is because H II regions and the DIG are distinct physical phenomena, rather than two ends of a continuous n_e distribution. We can take advantage of this bimodality to robustly separate the DIG from H II regions with an n_e threshold of $n_{e,\mathrm{thresh}} = 10\,\mathrm{cm^{-3}}$.
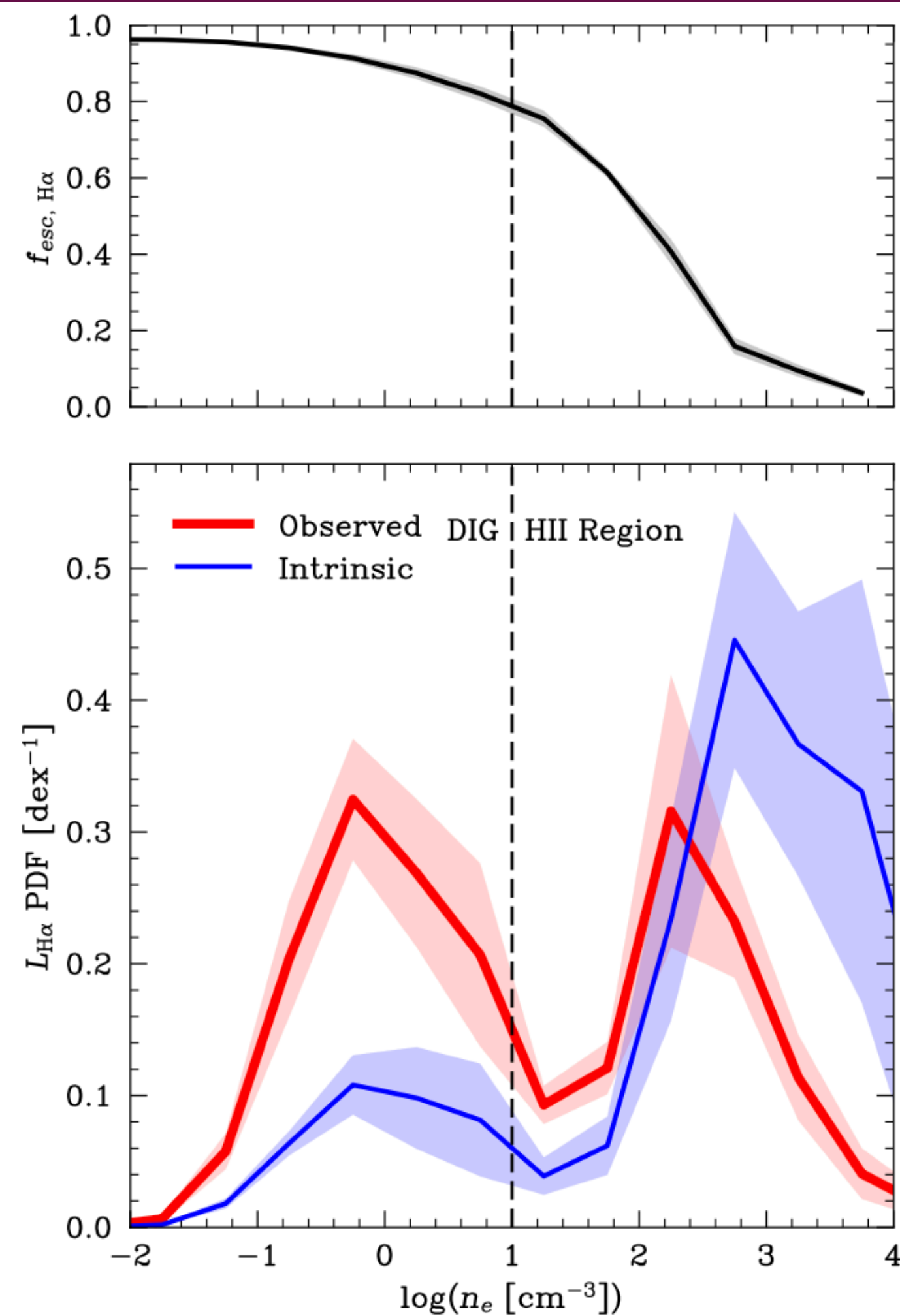

Figure 6. The emission and escape of $H\alpha$ emission in the DIG and H II regions. The trend lines and shaded regions represent the mean and standard deviation across four snapshots. *Top:* The escape fraction of $H\alpha$ as a function of n_e. We can see that H II regions are intrinsically much brighter than the DIG, however the observed luminosities are comparable due to much higher dust attenuation in H II regions causing low escape fractions. *Bottom:* The distribution of intrinsic and observed $H\alpha$ luminosity of gas cells in the MW-like simulation as a function of n_e. We can see bimodality in both the intrinsic and observed L_{H_α}, with two peaks at densities of $0.1 - 1\,\mathrm{cm^{-3}}$ and $10^2 - 10^3\,\mathrm{cm^{-3}}$. This motivates our use of $10\,\mathrm{cm^{-3}}$ as an electron density threshold between the DIG and H II regions.

4.2 Line ratios in the DIG

The immediate question to answer is whether the trends in the line ratios shown in Fig. 5 correspond to differences in line ratios between the DIG and H II regions, and to what extent the trends are merely artefacts of observational biases, such as projection effects, or due to physical processes, such as dust scattering.

To answer this, we analyze the gas by binning the cells according to n_e and calculating the observed luminosity for each bin. These luminosities enable us to calculate line ratios for the gas at each density. This is essentially the theoretical analogue of the surface brightness plots in Fig. 5.

In Fig. 7, we show the line ratios against n_e and confirm that the observed trends in these line ratios indeed correlate with changes in ionised gas density, particularly with decreasing n_e. We have not plotted the intrinsic line ratios as they are nearly indistinguishable from the observed line ratios since dust attenuation has little impact on the ratio of two lines with similar wavelengths.
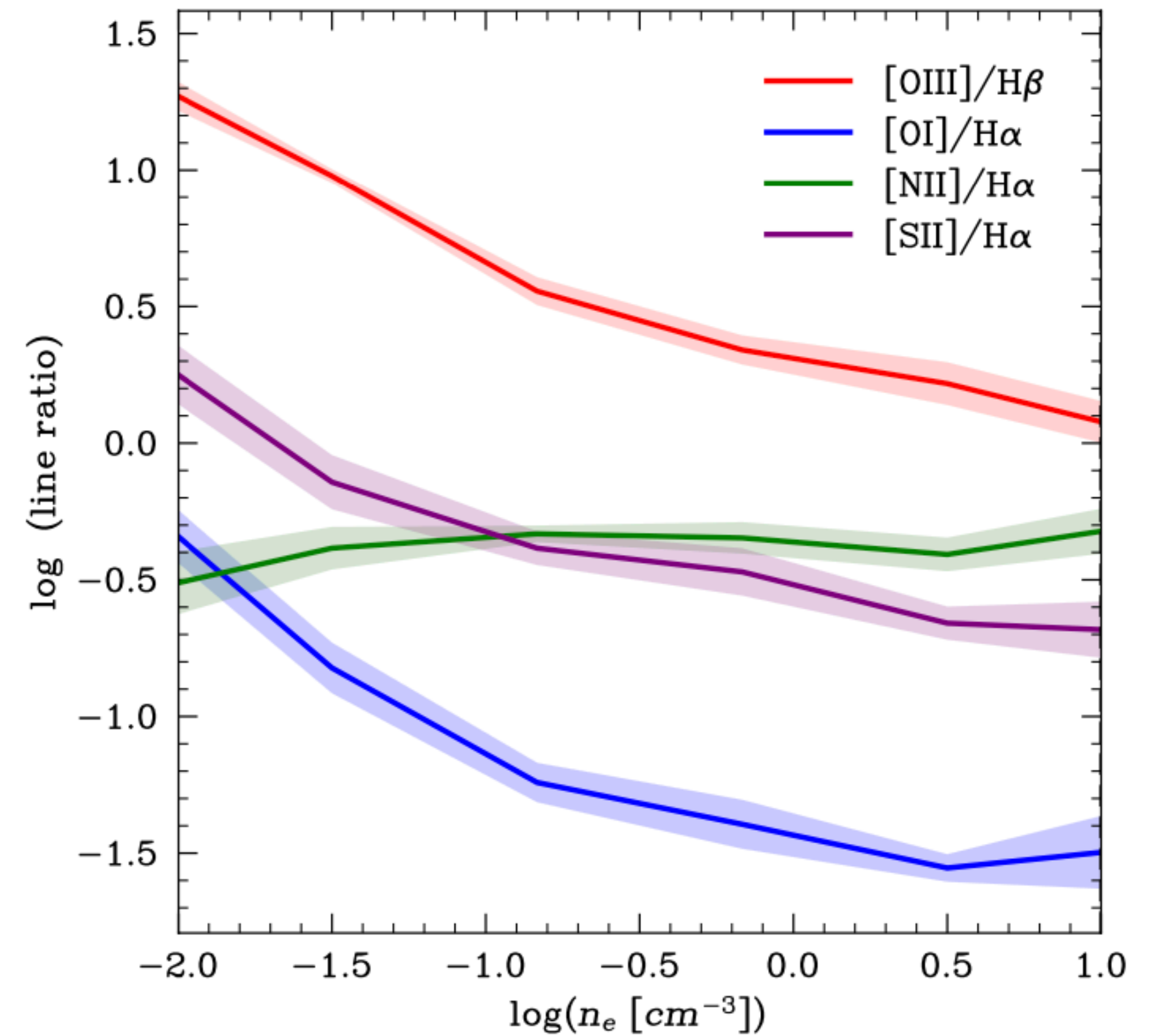

Figure 7. The [S II]/Hα, [N II]/Hα, [O I]/Hα, and [O III]/Hβ line ratios as a function of n_e. The trend line and shaded region represent the mean and standard deviation (in log space) across four snapshots. Line ratios were calculated by summing the observed luminosity in a metal emission line of all gas cells in the density bin, and then dividing by the summed observed luminosity of Hα or Hβ as appropriate. We can clearly see the same line ratio trends as in Fig. 5, however with a much steeper slope.

12

4.3 Explaining line ratios in the DIG

Having shown that [S II]/Hα, [O I]/Hα, and [O III]/Hβ intrinsically increase as the ionised gas becomes more diffuse, rather than being driven by observational biases, we can now explore how these trends arise.

Line ratios are fundamentally dependent on two factors; the relative emissivity of the emission lines and the relative abundance of the ions which give rise to the line ratios. As discussed in Section 1, both of these factors have been considered but it has been difficult to disentangle the degeneracy between them through observations. Fortunately, with our post-processing approach, we are able to disentangle the impacts of emissivity and abundance.

We will first consider the impact of relative abundance, and so in Fig. 8 we show the abundance of S^+, O^0, N^+, and O^{++} relative to H^+ as a function of n_e. Interestingly, we find that the O^0/H^+, S^+/H^+, and O^{++}/H^+ ratios all increase with decreasing n_e, which matches the trends of their respective line ratios. However, the shape of these curves does not match exactly with the line ratio trend. Conversely, the N^+/H^+ ratio decreases with decreasing n_e, whereas the trend of [N II]/Hα is flat. This indicates that the abundance ratios alone do not tell the full story and that emissivity must also be considered.

In discussing these line ratio trends, it is important to note that collisional ionisation and the UV background have a negligible impact. Charge exchange is dominant for the ionisation of O^0, subdominant for N^+, and unimportant for S and O^{++}. This means that photoionisation is the primary ionisation source for N^0, S^0, and O^{++}. The rising O^{++}/H^+ with decreasing n_e is a clear indicator of the hardening radiation field with decreasing n_e, and we will investigate the causes of this in Section 4.4.
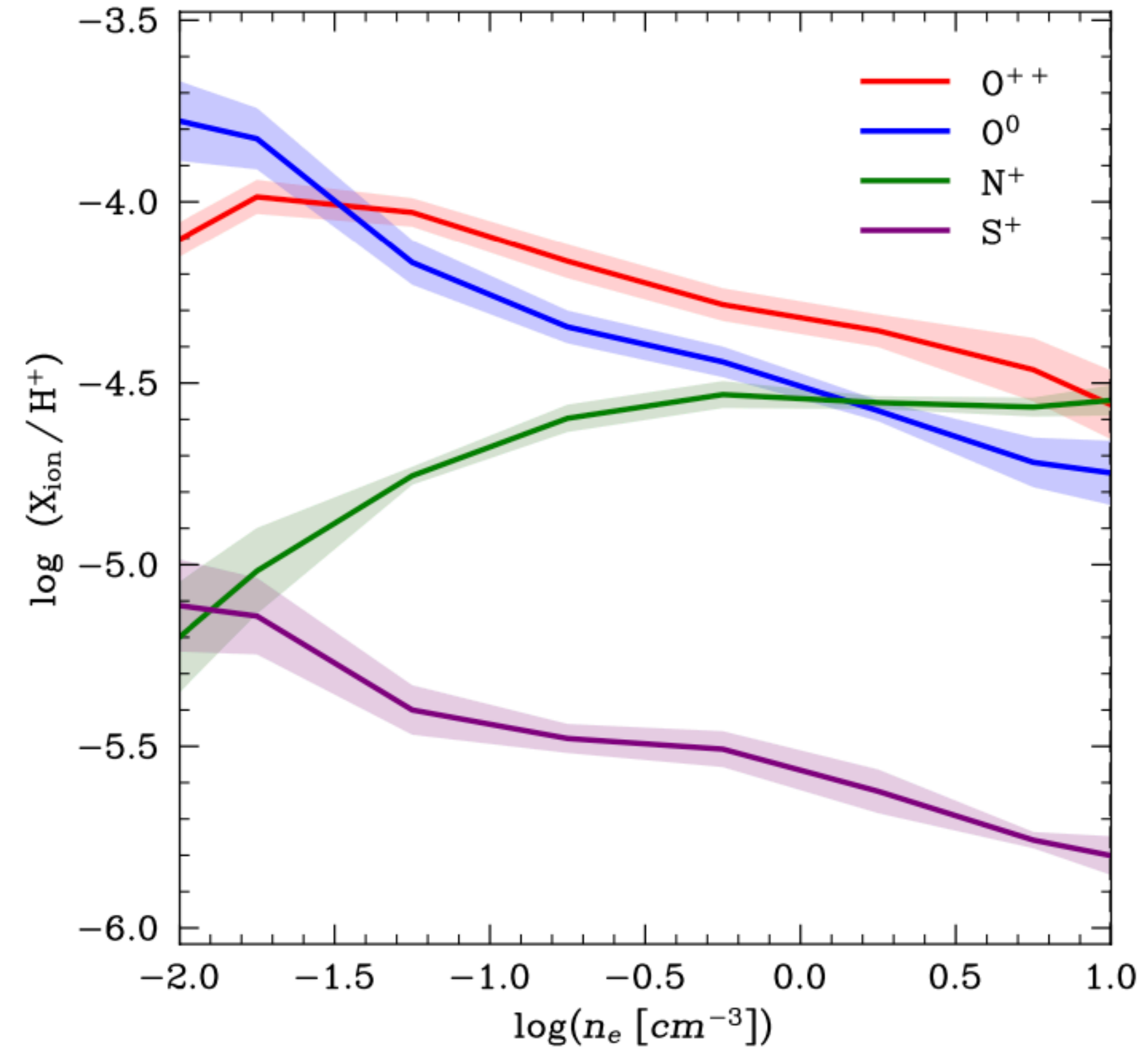

Figure 8. The abundance of S^+, O^0, N^+, and O^{++} relative to H^+ is shown as a function of n_e. The trend line and shaded region represent the mean and standard deviation across four snapshots. S^+/H^+, O^0/H^+, and O^{++}/H^+ all increase with decreasing n_e, consistent with the trends of their line ratios, [S II]/Hα, [O I]/Hα, and [O III]/Hβ, although with different magnitudes and curvature. N^+/H^+ decreases with decreasing n_e, in contrast to the flat [N II]/Hα trend. This shows the importance of jointly considering emissivity (Fig. 9) and abundances (shown here).

In Fig. 9 we show the change in relative emissivity for the line ratios. The emissivity ratios considered increase with decreasing n_e because of increasing temperature in the DIG with decreasing n_e.

The temperature increase causes a more rapid increase in emissivity for CELs than for RLs such as Hα and Hβ. The temperatures of our DIG are consistent with the observed DIG in the Milky Way. Madsen et al. (2006) find that the DIG within the Milky Way is in the range of $[7000 - 10\,000]$ K, with an average of 9000 K. We find the average temperature of our DIG is 9000 K when weighted by observed Hα emission to account for observability. Fig. 9 also shows that the vast majority of luminous gas (see Fig. 6) is within observed Milky Way DIG temperature ranges. The important insight here is that the trend of increasing temperature with n_e is enough to boost the relative emissivity of the line ratios with decreasing n_e.
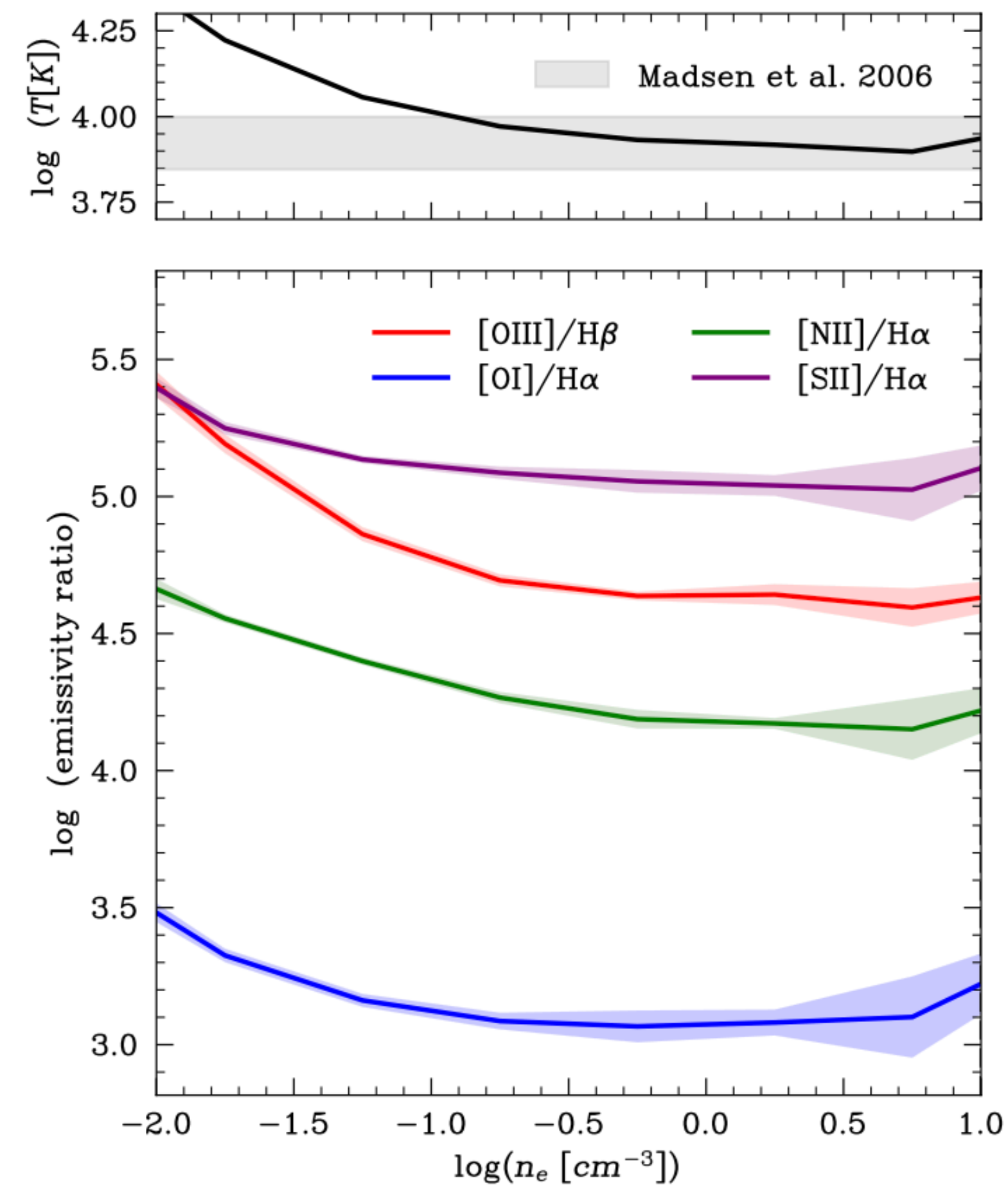

Figure 9. A comparison of the effective relative emissivity of the [S II]/Hα, [N II]/Hα, [O I]/Hα, and [O III]/Hβ line ratios. The trend line and shaded region represent the mean and standard deviation across four snapshots (in log space). *Top:* The average temperature of gas weighted by observed Hα flux. The grey band shows the range of DIG temperatures observed in the Milky Way by Madsen et al. (2006). This shows that the temperature of the observable DIG is consistent with the observed DIG temperature. *Bottom:* The relative emissivity of the line ratios generally increases with decreasing n_e due to the collisionally excited metal lines being more sensitive to the increasing temperature in the DIG. The changing emissivity is vital to drive the line ratio trends in Fig. 7, together with the abundances shown in Fig. 8.

4.4 Source of ionising photons

We now aim to understand the hardening of the radiation field with decreasing n_e, which is implied by the changes in ionic abundances presented in Fig. 8. We focus on the hardening of radiation in the DIG in reference to the fraction of photons with energy above the ionisation energy of O^{++}, 35.12 eV. Quantities regarding hard ionising photons with energy above 35.12 eV are denoted with subscript h, whereas rates regarding all ionising photons with energy above 13.6 eV are denoted with subscript 0.

Two primary mechanisms could account for this hardening of the radiation field with decreasing n_e: either the ionising radiation emitted from sources in the dense gas (e.g. young stars in H II regions) becomes harder as it travels into the DIG, or the intrinsic hardness of the ionising sources change because of a relative change in the contribution from stars of different ages.

Due to our Monte Carlo approach, we can trace the source of each photon absorbed in the gas cells. This allows us to dissect the
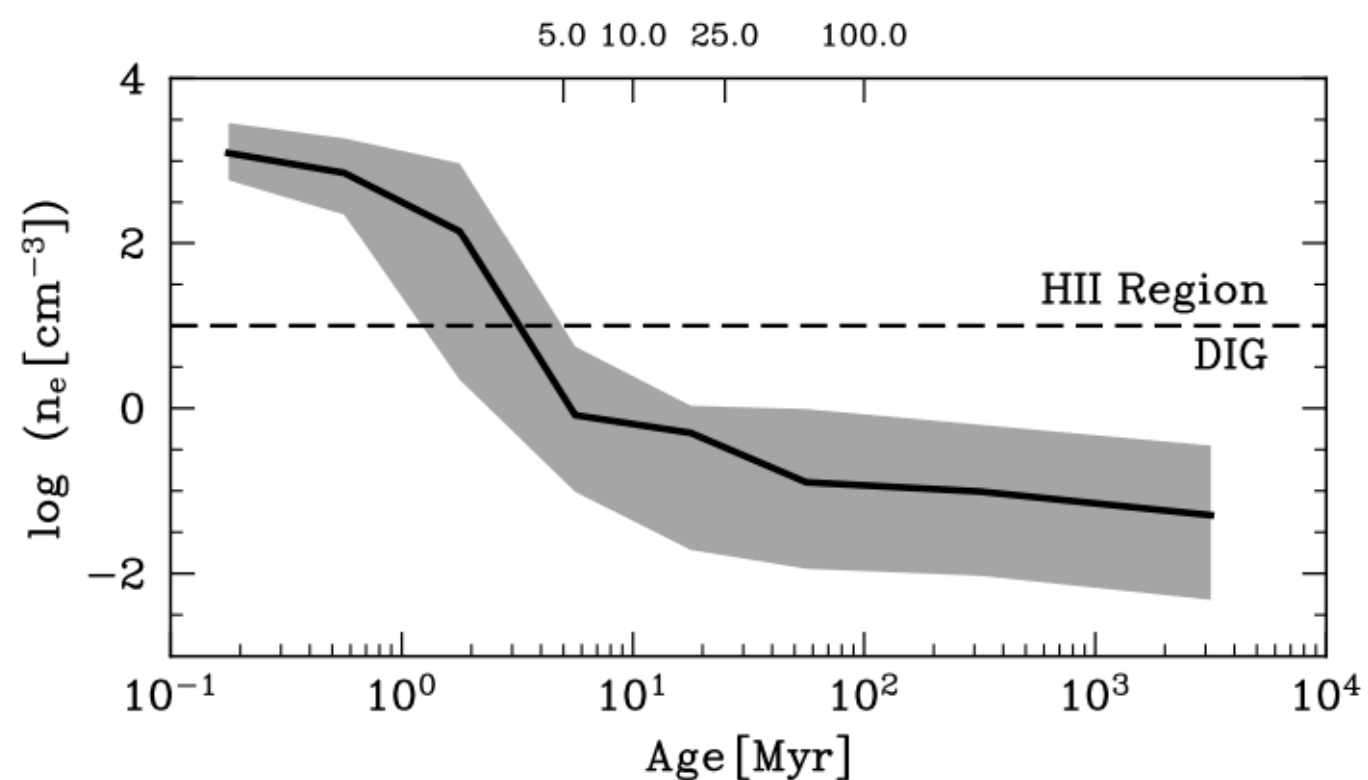

Figure 10. The evolution of the ionising radiation field with n_e. The trend line and shaded region represent the mean and standard deviation across four snapshots. *Top:* The rate of photoionisations due to photons above the H I ionisation energy (13.6 eV) for a given age bin, Γ_0, normalised by the total number in the simulation, $\sum \Gamma_0$. Stars aged younger than 5 Myr are the dominant source of ionisation in H II regions. As n_e decreases, there is a transition of the dominant ionising source to older stars. *Bottom:* The rate of photoionisations due to photons above the O II ionisation energy (35.12 eV), Γ_h, divided by Γ_0. The ionising radiation field becomes harder with decreasing n_e because the dominant source of ionising radiation transitions to older stars which have intrinsically harder SEDs.

Figure 11. The median n_e of gas immediately surrounding stars of different ages. Shaded regions represent the 16-84th percentile scatter. Stars have cleared their dense H II regions by ~ 5 Myr age through radiation pressure and nearby supernovae. This exposes them to the DIG while they are still emitting a copious amount of ionising radiation, allowing stars of ages between 5 and 25 Myr to ionise the DIG.
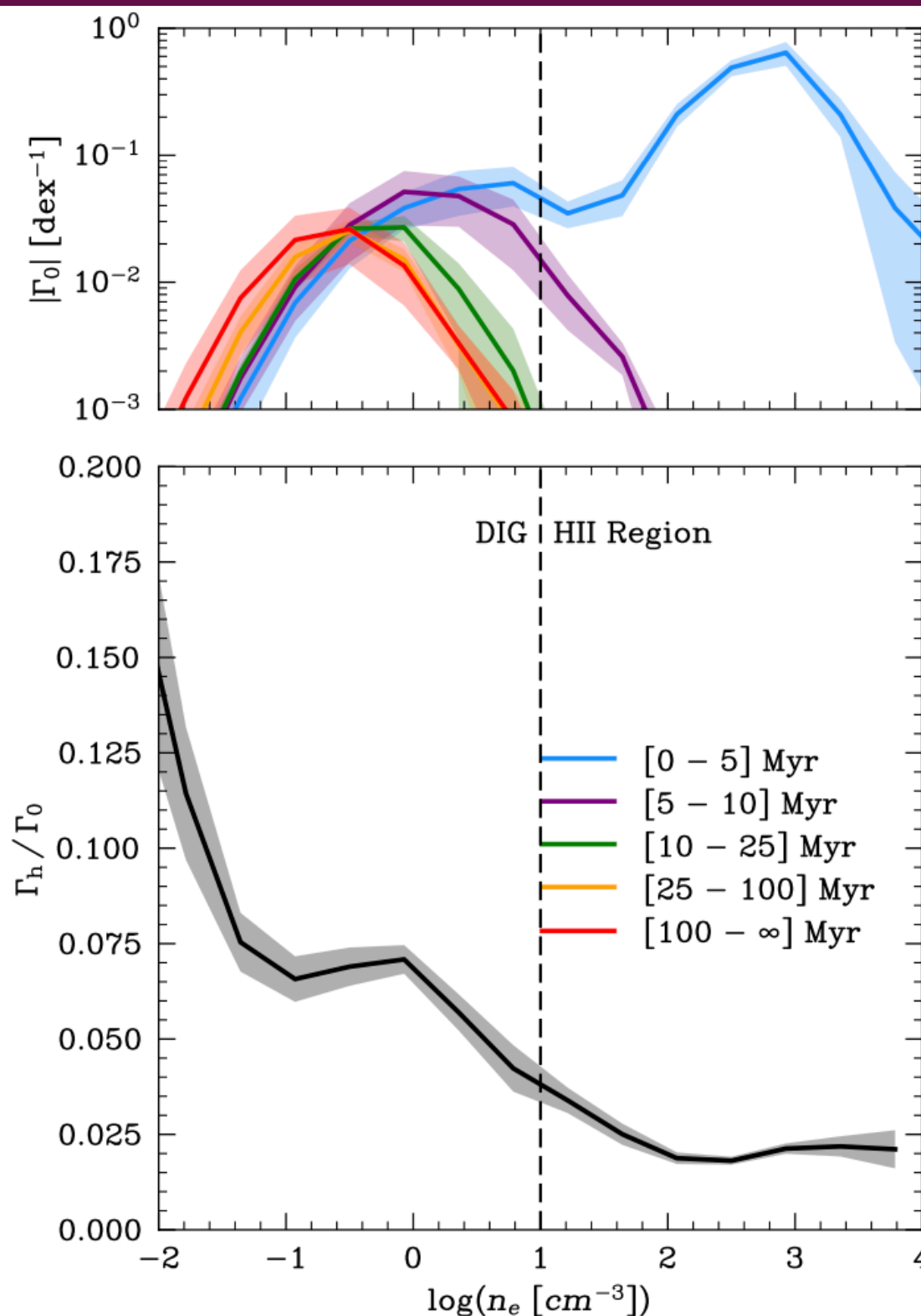
When considering the roles of these different populations, we can understand how the radiation field hardens as the gas becomes more diffuse. Very young stars (<5 Myr) are nearly entirely responsible for the ionisation of H II regions, however radiation leaking from these H II regions contributes modestly to the overall ionisation of the DIG (26%) and is a small contribution to the hard radiation absorbed in the DIG (12%). After ~ 5 Myr, the H II regions are dispersed by feedback from the massive stars and nearby supernovae, meaning that this population is situated in the DIG. The clearing of H II regions coincides with an uptick in hardness of the intrinsic SED, allowing these still young and luminous stars to propagate a hard radiation field into the DIG.

As the stars age, their ionising SED hardens and they emit less ionising radiation. We can see in the top panel of Fig. 10 that the [0 − 5] Myr, [5 − 10] Myr, and [10 − 25] Myr populations are dominant in increasingly diffuse gas as their star formation sites become disrupted by stellar feedback and they are more firmly situated in diffuse gas. As the intrinsic hardness of the radiation also increases from [0 − 5] Myr, [5 − 10] Myr, to [10 − 25] Myr, this causes the a hardening of the radiation field. The ionising output of the stars falls off rapidly such that all stars above 25 Myr contribute only relatively modestly to DIG ionisation, and are not functionally important for ionising the DIG.

The [100 − ∞] Myr population includes many different types of stars, but most notably the HOLMES or post-AGB stars which are thought to release a significant amount of hard ionising photons. Although the age range of this population is broad and includes stars which may not usually be thought of as "old", it is appropriate for our purposes because we are still separating the HOLMES from other potentially important populations. The oldest stars in this population emit the hardest radiation, particularly at ages greater that 1 Gyr, as seen in the bottom panel of Fig. 12. However, we find that these stars are only a very minor contribution to the ionising radiation field in the DIG, primarily because of the very low intrinsic ionising luminosity.

The line ratio trends, in particular the increase in [O III]/Hβ with decreasing n_c, implies hardening ionising radiation in the DIG. The favoured explanation for this has been the presence of HOLMES in the DIG which comprise a small fraction of the overall ionisation, but emit an outsize amount of high energy photons (Zhang et al. 2017; Belfiore et al. 2022). We instead find that the ionisation of the DIG is driven by stars of ages between 5 and 25 Myr, which have generally cleared their H II regions and emit hard ionising radiation.

The hardened radiation in the [5−25] Myr age range is caused by Wolf-Rayet (WR) phase stars. WR stars are hotter than O type stars, and thus emit harder ionising radiation. Importantly, the BPASS stellar models used in this study account for the creation of WR stars through binary interactions which strip the hydrogen envelope of cool red supergiants, which creates many more WR stars at older ages (up to ∼100 Myr) compared to single-star modelling (Xiao et al. 2018).

Using the single-star Bruzual & Charlot (2003) (BC03) model instead would lead to ∼2 orders of magnitude less intrinsic ionising luminosity for the [10−100] Myr stars. Interestingly, Fig. 12 shows
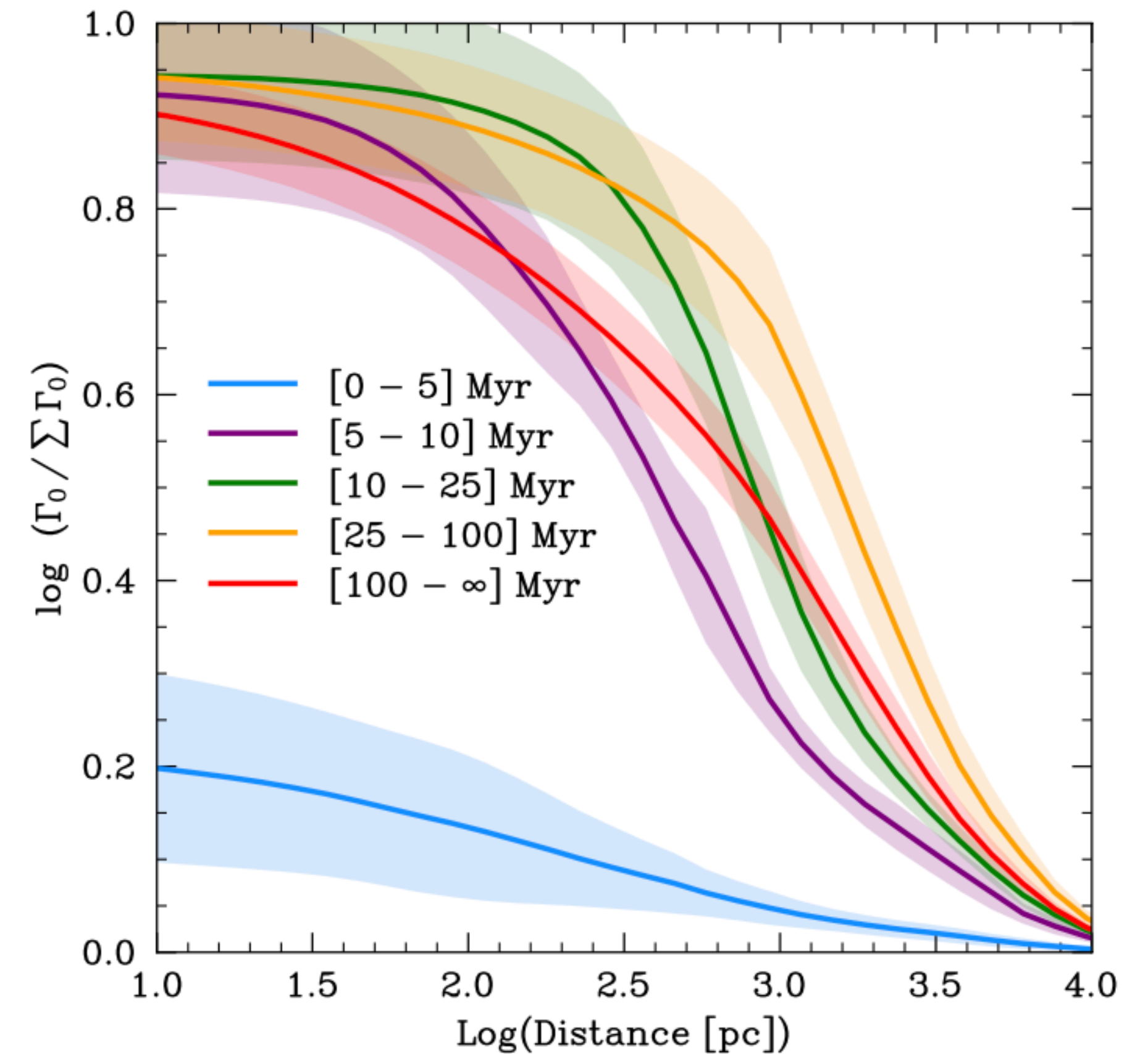

Figure 13. The fraction of ionising photons which have not yet been absorbed as function of distance from the source star. The trend line and shaded region represent the mean and standard deviation across four snapshots. Stars younger than 5 Myr emit ionising photons which are mostly absorbed on small scales (<1 pc), however photons which leak from H II regions can propagate on kpc scales. More importantly, ionising photons from stars older than 5 Myr propagate across scales up to 10 kpc. This long mean free path allows stars of ages between 5 to 25 Myr to ionise the DIG on galactic scales.

6 CONCLUSIONS

We have undertaken a pioneering self-consistent galaxy-scale study of the ionisation and emission from the diffuse ionised gas in star-forming galaxies. This level of detailed modelling is necessary to capture the interplay of different stellar populations, the complex radiative transfer effects, and the varied heating sources present throughout the ISM.

Our analysis is based on a high-resolution simulation of a Milky Way-like galaxy, which includes state-of-the-art physics such as multi-band on-the-fly radiative transfer, dust formation and destruction, and a realistic stellar feedback subgrid recipe. We employed the Monte Carlo radiative transfer (MCRT) code COLT to post-process the radiative transfer of ionising and emission line photons, and we carefully compared our mock observations to MaNGA and to ~10 pc resolution MUSE emission line maps to confirm that we produce a physically realistically DIG in emission (Fig. 5).

Our main conclusions are summarised as follows:

(i) The DIG and H II regions are distinct when the observed $L_{H\alpha}$ from gas cells is plotted against electron density, n_e, as we can see that the bulk of observed Hα emission is due to two peaks at $0.1-1$ cm^{-3} and 10^2-10^3 cm^{-3} (Fig. 6). We use this bimodality to define the DIG/H II region threshold as $n_e = 10$ cm^{-3}.

(ii) The observed trends in [S II]/Hα, [N II]/Hα, [O I]/Hα, and [O III]/Hβ with decreasing surface brightness correspond to genuine trends in these emission line ratios as ionised gas becomes more diffuse; i.e. with decreasing n_e (Fig. 7). These trends are caused by a combination of changing relative emissivity and relative abundances with decreasing n_e.

(iii) The relative emissivity of the [S II]/Hα, [N II]/Hα, [O I]/Hα, and [O III]/Hβ line ratios increase with decreasing n_e due to an increasing temperature with decreasing n_e (Fig. 9). The increase in O^{++} relative to H$^+$ with decreasing n_e is caused by the radiation field becoming harder with decreasing n_e.

(iv) The DIG is primarily ionised by radiation from stars recently formed stars of ages between 5 and 25 Myr. Ionisation of the DIG by these stars is primarily possible due to clearing of H II regions by ~ 5 Myr (Fig. 11), exposing bright young stars directly to the DIG, rather than bona fide leakage through dense H II regions (Fig. 10).

(v) As stars age from 0 to 25 Myr, they emit increasingly hard ionising radiation (Fig. 12) and they become situated in increasingly diffuse regions of gas. This causes the average age of stars responsible for ionising the gas to increase with decreasing n_e, and therefore the hardening of ionising radiation with decreasing n_e (Fig. 10).

(vi) The line ratio trends in the DIG can be explained as a direct consequence of ongoing star-formation, rather than needing to invoke a secondary ionisation source such as HOLMES. Variation in the precise star-formation history over the last 25 Myr may explain the scatter in the observed line ratio trends between galaxies.

(vii) Once the H II region around a young star has been cleared, it is able to ionise gas on galaxy-wide scales (Fig. 13). This provides a plausible explanation for the relative uniformity (relatively small scatter) of line ratio trends radially within individual galaxies, after accounting for metallicity gradients.

The persistence of high altitude non-equilibrium diffuse ionized gas in simulations of star forming galaxies

Lewis McCallum,[1] Kenneth Wood,[1] Robert Benjamin,[2] Camilo Peñaloza,[1] Dhanesh Krishnarao,[3] Rowan Smith,[1] Bert Vandenbroucke[4]

[1] *School of Physics and Astronomy, University of St Andrews, North Haugh, St Andrews, KY16 9SS, UK*
[2] *Department of Physics, University of Wisconsin-Whitewater, Whitewater, WI 53190, USA*
[3] *Department of Physics, Colorado College, Colorado Springs, CO 80903, USA*
[4] *Leiden Observatory, Leiden University, PO Box 9513, 2300 RA Leiden, the Netherlands*

ABSTRACT
Widespread, high altitude, diffuse ionized gas with scale heights of around a kiloparsec is observed in the Milky Way and other star forming galaxies. Numerical radiation-magnetohydrodynamic simulations of a supernova-driven turbulent interstellar medium show that gas can be driven to high altitudes above the galactic midplane, but the degree of ionization is often less than inferred from observations. For computational expediency, ionizing radiation from massive stars is often included as a post-processing step assuming ionization equilibrium. We extend our simulations of a Milky Way-like interstellar medium to include the combined effect of supernovae and photoionization feedback from midplane OB stars and a population of hot evolved low mass stars. The diffuse ionized gas has densities below $0.1 \, \mathrm{cm}^{-3}$, so recombination timescales can exceed millions of years. Our simulations now follow the time-dependent ionization and recombination of low density gas. The long recombination timescales result in diffuse ionized gas that persists at large altitudes long after the deaths of massive stars that produce the vast majority of the ionized gas. The diffuse ionized gas does not exhibit the large variability inherent in simulations that adopt ionization equilibrium. The vertical distribution of neutral and ionized gas is close to what is observed in the Milky Way. The volume filling factor of ionised gas increases with altitude resulting in the scale height of free electrons being larger than that inferred from $\mathrm{H}\alpha$ emission, thus reconciling the observations of ionized gas made in $\mathrm{H}\alpha$ and from pulsar dispersion measurements.

Key words: methods : numerical – ISM : structure – galaxies : ISM – galaxies : star formation – ISM : kinematics and dynamics – ISM : HII regions